nature materials

Article

https://doi.org/10.1038/s41563-024-01963-4

Atomically precise inorganic helices with a programmable irrational twist

Received: 20 December 2022

Accepted: 2 July 2024

Published online: 26 July 2024

Check for updates

Dmitri Leo Mesoza Cordova ® ^{1,4}, Kenneth Chua ^{1,4}, Tyler A. Kerr ® ¹, Toshihiro Aoki ® ², David Knez ® ¹, Grigorii Skorupskii ³, Diana Lopez ® ¹, Joseph Ziller ¹, Dmitry A. Fishman ® ¹ & Maxx Q. Arguilla ® ¹ ⊠

Helicity in solids often arises from the precise ordering of cooperative intra- and intermolecular interactions unique to natural, organic or molecular systems. This exclusivity limited the realization of helicity and its ensuing properties in dense inorganic solids. Here we report that Ga atoms in GaSel, a representative III–VI–VII one-dimensional (1D) van der Waals crystal, manifest the rare Boerdijk–Coxeter helix motif. This motif is a non-repeating geometric pattern characterized by 1D face-sharing tetrahedra whose adjacent vertices are rotated by an irrational angle. Using InSel and GaSel, we show that the modularity of 1D van der Waals lattices accommodates the systematic twisting of a periodic tetrahelix with a 4_1 screw axis in InSel to an infinitely extending Boerdijk–Coxeter helix in GaSel. GaSel crystals are non-centrosymmetric, optically active and exfoliable to a single chain. These results present a materials platform towards understanding the origin and physical manifestation of aperiodic helicity in low-dimensional solids.

Encoding helicity onto dense inorganic lattices is a non-trivial process. While these motifs are pervasive in nature and organic-based structures, the lack of cooperative bonding modalities that induces twisting in one-dimensional (1D) structures such as hydrogen bonding, disulfide bridging, and π - π stacking makes it challenging to impart helicity in solids composed of only densely packed inorganic atoms¹⁻³. The exclusive dependence of solid-state crystalline structure and atomic-scale packing on the local bonding environment and atomic radius ratios has, therefore, limited the realization of helicity in engineered systems to the mesoscale and nanoscale. Beyond the novelty of long-range helical structures, the chiral and nonlinear nature of helices at the atomic scale has protracted the desire towards designing helical structures to realize emergent electronic and optical phenomena^{4,5}. The absence of a centre of inversion, which often accompanies a highly nonlinear structure at the atomic scale such as a helix, has been postulated to host sought-after phenomena such as long-range spin polarization via chiral-induced spin selectivity, subnanoscale chiroptics, circularly polarized light emission and absorption, and topologically non-trivial helicoid states in dense solids⁶⁻⁸.

Discovery of helical materials at the atomic scale

In the mesoscale down to the nanoscale, engineered helicity and chirality have only been achieved through the precise programming of chiral topological defects such as axial screw dislocation-induced Eshelby twisting or via well-defined face-sharing assembly of tetrahedral nanocrystal superstructures 9-14. Attempts towards the creation of extended inorganic structures bearing helical motifs defined at the atomic scale have been limited to polygonal helical structures and unique double helices such as the Sn(VII)P (VII = Br, I) phases that bear motifs that are exceedingly scant in engineered solids¹⁵⁻¹⁷. Generally, these structures result from an underlying crystallographic, n_m , screw axis symmetry element that corresponds to a 360°/n rotation followed by an *m/n* unit-cell translation that arises from long-range packing and secondary molecular structures (Fig. 1a)¹⁸⁻²¹. In face-sharing tetrahedral helical chains generally referred to as tetrahelices, the structure is defined by a periodic order that repeats every four atomic layers with its symmetry arising from the combination of a 90° rotation and 1/4 unit translation about the principal axis. In most reported crystals, this 41 screw axis symmetry consequently produces periodic tetrahelix rods

Department of Chemistry, University of California Irvine, Irvine, CA, USA. ²Irvine Materials Research Institute, University of California Irvine, Irvine, CA, USA. ³Department of Chemistry, Princeton University, Princeton, NJ, USA. ⁴These authors contributed equally: Dmitri Leo Mesoza Cordova, Kenneth Chua. ©e-mail: marguill@uci.edu

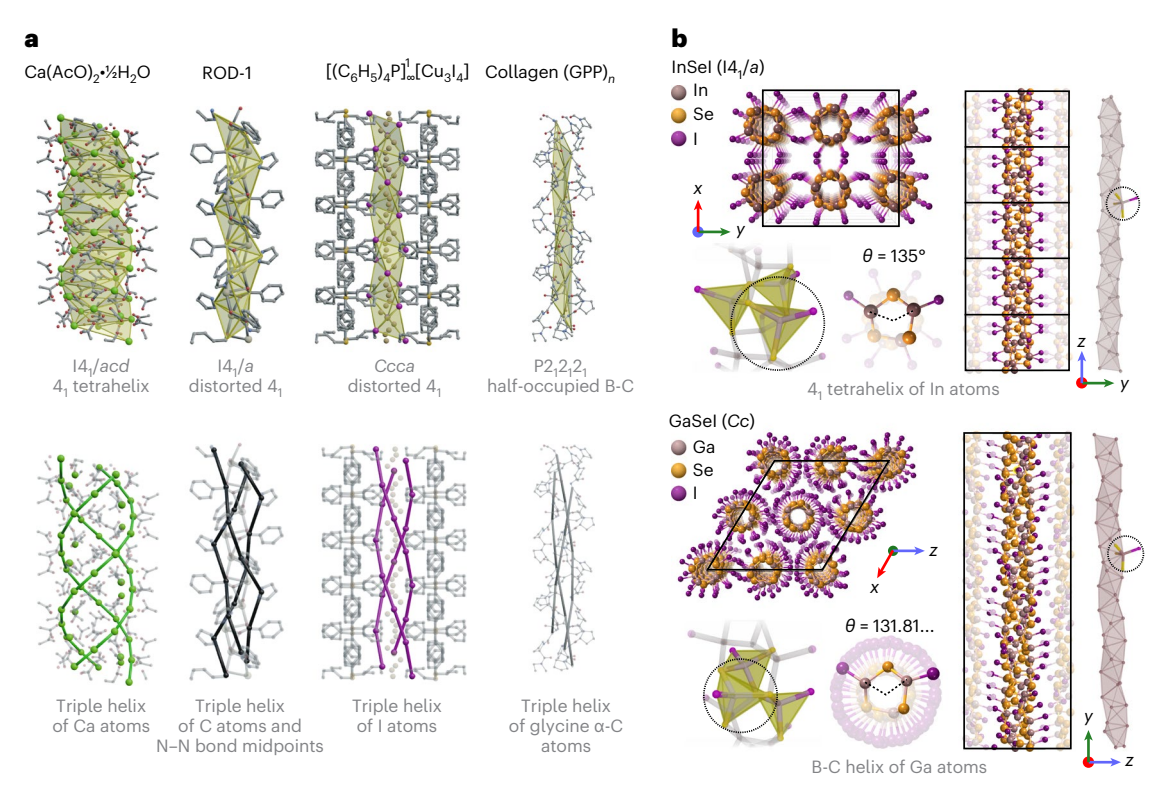


Fig. 1| **Helices possessing rational and irrational twist angles. a**, Top: crystal structures of extended molecular lattices with tetrahelix motifs characterized by the non-distorted (Ca(AcO) $_2$ -1/2 H_2 O) ¹⁸ and distorted (ROD-1and [(C₆ H_3) $_4$ P] $_\omega$ ¹[Cu $_3$ I₄]) $_4$ 1 screw axis ^{19,20}, and a half-occupied B-C helix motif (for collagen (GPP) $_n$) ²¹. Bottom: the triple-helix traces. **b**, Top: crystal structures of helical 1D vdW lattices, InSel and GaSel. The unit cell of InSel is characterized by chains with a periodic 4_1 screw

axis motif defined by a 135° rotational angle between two distinct $16f \ln sites (\theta_t)^{32}$. Bottom: the unit cell of GaSeI that is composed of chains with quasi-tetrahedral Ga central atoms (brown) that manifest ideal B-C helicity with the corresponding θ_r highlighted. Wire frame structures represent the [InSe₃I]_∞ and [GaSe₃I]_∞ quasi-tetrahedral units (dashed circles) of InSeI and GaSeI, respectively.

that, in helical parameters, corresponds to a repeating rotational or twist angle of 135° between consecutive atomic layers.

Of these polygonal helices, the aperiodic tetrahelix analogue that can be geometrically defined from the same face-sharing tetrahedral motif by slightly twisting this rotation angle is sought after²²⁻²⁶. This densely packed tetrahelix known as a Boerdijk-Coxeter (B-C) helix is, like nucleic acids, an infinitely extending helix with either left- (L) or right (R)-handed chirality. Its aperiodicity and structural complexity that led to its paucity arise from the rotational advance of the face-sharing tetrahedron that comprises the tetrahedra that corresponds to $\pm \cos^{-1}(-2/3) \approx 131.81...^{\circ}$, an irrational number²⁶. The irrational rotational angle of the B-C helix means that the structure possesses no translational symmetry and does not repeat along the chain axis. Due to the strict adherence of the B-C helix to the 131.81...° rotational angle, this aperiodic helical motif has long been elusive in the atomic scale. Thus, the B-C helix has only been postulated to exist in main group elements and has only been demonstrated as non-ideal variants emerging from secondary structures in collagen, sublattice motifs in intermetallics, or macroscale structures inspired by Buckminster Fuller's tetrahelix tower such as Art Tower Mito in Ibaraki, Japan^{22,27}. So far, there has not been any conclusive evidence that this motif exists in dense, freestanding and extended lattice structures. The aperiodic nature of B-C helices also makes them a potential geometric platform to explore pseudo-crystalline behaviour in a 1D form factor that is typically inaccessible at the atomic scale. The structural complexity of 1D crystals with quasi-periodic order offers a unique outlook into optical, photonic and topological phenomena as aperiodic crystals are poised to display unique higher-order structural complexity and order in Fourier space not observed in their periodic equivalents^{28–30}. Harnessing these traits in a 1D form factor approaching the atomic scale will open avenues to access properties driven by the interplay of aperiodicity, non-centrosymmetry and quantum confinement.

One-dimensional van der Waals (vdW) crystals consisting of covalently bound atomic chains held together by weak non-covalent forces are a suitable platform to explore the prospects of helicity in dense solids³¹. Owing to the highly anisotropic bonding nature in these solids. the concurrence of both crystallographic and non-crystallographic screw axes with a prominent lattice tractability in many of these phases allows for a structurally and chemically modular platform that can accommodate large lattice changes. Among classes of 1D vdW crystals, the group III-VI-VII (1:1:1) solids, often referred to as triel chalcohalides, are of specific interest due to the few reported crystal structures that range from 1D atomic tubules to two-dimensional (2D) phosphorene-like sheet morphologies^{32,33}. The low rigidity and unique structure afforded by its vertex-sharing quasi-tetrahedral polyhedral lattice make these materials potential candidates for optoelectronics³⁴, piezoelectrics³⁵, ferroelectrics^{36,37}, stimulus-responsive sensors³⁸ and even building blocks for spintronic applications^{39,40}. The most studied phase in this group is InSeI, an exfoliable, visible-range direct band gap semiconductor structurally characterized by a 1D covalent network composed of quasi-tetrahedral building blocks 32,34,38-41. While often overlooked and understudied in the context of structural helicity, InSeI is an ideal model system to probe atomic-scale helicity as its polymer-like covalent 1D structure exhibits an inherent 41 screw axis and a periodic tetrahelical rotational angle of 135° (Fig. 1b and Supplementary Text A).

Herein, we describe the systematic twisting of a periodic 4_1 tetrahelix that is based on the class of atomically precise III–VI–VII 1D vdW lattices into a structure that manifests the ideal B-C helix motif. We demonstrate this by substituting a smaller Ga atom into

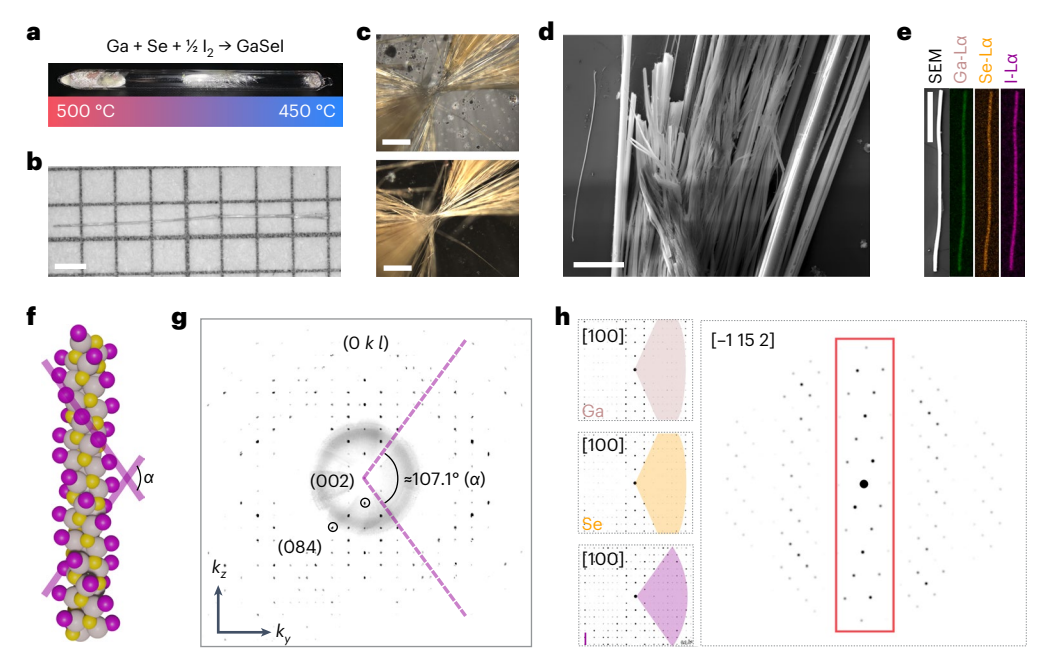


Fig. 2 | **Synthesis and single-crystal structure of GaSel. a**, CVT synthesis of GaSel crystals. **b**, Sizeable needle-like crystal of GaSel. Scale bar, 1 mm. **c**, Bright (top) and dark (bottom) field images of GaSel crystals exhibiting radial crystal growth. Scale bars, 225 μ m. **d**, SEM of fibrous GaSel crystallites. Scale bar, 10 μ m. **e**, SEM and EDS elemental maps of GaSel. Scale bar, 10 μ m. **f**, Model of a single GaSel chain. The meridian angle, α , arising from the crossing of the iodine helix is

depicted in purple. \mathbf{g} , Experimental single-crystal precession diffraction image of GaSel along the $(0 \, k \, l)$ plane. \mathbf{h} , Simulated SCXRD patterns representing the elemental contributions oriented along the $[1 \, 0 \, 0]$ zone axis (left) and the overall GaSel projection along the $[-115 \, 2]$ zone axis (right). Meridian angles arising from the Ga, Se and I helices are shown in brown, yellow and purple, respectively.

the quasi-tetrahedrally coordinated In site in InSel 32 (Fig. 1b, top) to form GaSel, an exfoliable 1D helical crystal characterized by counter-propagating helical chains that are held together by weak vdW forces (Fig. 1b, bottom). We found that Ga substitution, coupled with the structural degree of freedom afforded by weak interchain vdW interactions, results in the twisting of the 135° periodic 4_1 tetrahelix rotational angle in InSel into the elusive B-C helix rotational angle of -131.81...° in Ga tetrahelices in GaSel. While GaSel is composed of racemic helices, the manifestation of B-C helicity lends to its organization into a phase with a non-centrosymmetric Cc space group.

Solid-state synthesis and structural characterization of 1D vdW helices

The high vapour pressures of Se and I transport agents facilitated the gram-scale synthesis of long and temperature-stable crystals of phase pure GaSel from elemental precursors using chemical vapour transport (CVT) under a 50 °C temperature gradient (Fig. 2a and Supplementary Fig. 1). Isolatable white- to beige-coloured crystals of GaSel deposited in the cold end of the reaction tube as long flexible needles reaching lengths of up to 0.8 cm (Fig. 2b). Bright- and dark-field optical micrographs taken from unperturbed crystals along the wall of the reaction tube highlight the radial growth habit of GaSeI, a crystallization motif commonly found in crystals and minerals with underlying 1D ordering (Fig. 2c). High-magnification scanning electron microscopy (SEM) of micromechanically spread GaSeI needles across a Si/SiO₂ substrate showed the highly fibrous microstructure arising from the weak interchain vdW bonding interactions (Fig. 2d). Resulting spectrographs and elemental maps from energy-dispersive X-ray spectroscopy (EDS) and mapping on isolated microcrystals show the expected ~1:1:1 ratio of Ga, Se and I atoms and the uniform distribution of these elements across the length of the crystal, consistent with X-ray photoelectron spectroscopy (XPS) results (Fig. 2e, Supplementary Figs. 2 and 3, Supplementary Tables 1 and 2 and Supplementary Text B). We established using thermogravimetric analysis (TGA) that GaSeI is thermally stable

under inert air conditions up to 422 °C (695.15 K) (Supplementary Fig. 4). From temperature-dependent micro-Raman studies, we do not observe structural phase transitions that occur from -189.15 °C (84 K) to room temperature (Supplementary Fig. 5).

Refinement of the single-crystal X-ray diffraction (SCXRD) data collected at -180.15 °C (93 K) combined with the compositional and elemental information collected from GaSeI crystals reveal that GaSel crystallizes in a non-centrosymmetric monoclinic space group Cc (no. 9; Fig. 1b, bottom, Supplementary Fig. 6, Supplementary Tables 3-7 and Supplementary Text C and D). The refined structure is composed of GaSeI L- and R-handed helical chains that counter-propagate along the crystalline b axis. These alternating R- and L-handed chains pack into a pseudo-hexagonal lattice. These chains are built from a repeating structure of quasi-tetrahedrally coordinated central Ga atom bound to three Se atoms and one latom (Fig. 1b, bottom, and Supplementary Figs. 7 and 8). Here, Ga and Se atoms assemble as a cylindrical network that propagates along the long axis of the crystal while the I atoms are oriented lateral of this cylinder. Close inspection of the nearest interchain I-I distances (3.665 Å; Supplementary Table 8) derived from the refined structure reveals that these correspond to distances that approach twice the vdW radius of I, confirming that the GaSeI chains are held together by weak vdW interactions. Whereas the chirality of the GaSeI helices alternates along the crystallographic c axis ([001] zone axis), the helices are organized into rows of the same chirality/handedness along the perpendicular (a) axis ([100] zone axis) (Supplementary Fig. 8), making facet-selective exfoliation a latent strategy to expose chiral and enantiopure facets that are composed of helices with identical handedness as is observed in its closely related, periodic analogue, InSel^{39,42}.

We employed a total least-squares method traditionally used to define the helicity of proteins and nucleic acids to fit the helical parameters of constituent atoms and to gain further insights on the helicity of GaSel (Fig. 2f) 43 . Using the HELFIT software, we were able to extract the constituent types I and III (Supplementary Text E) periodic helical

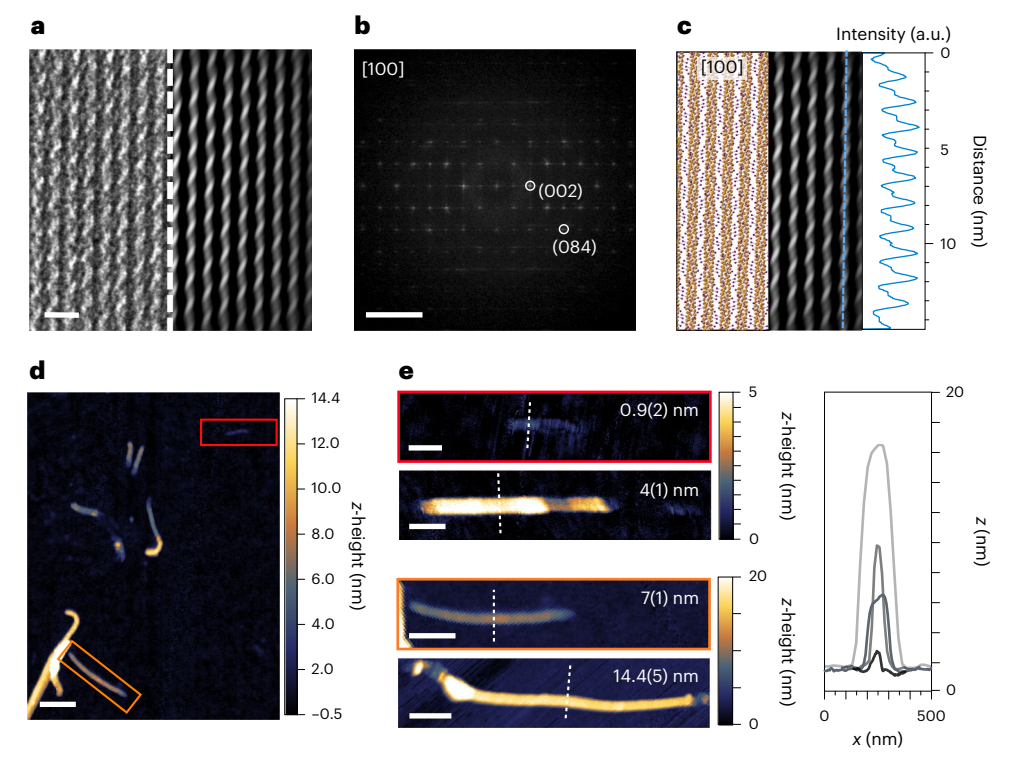


Fig. 3 | Microstructure and nanoscale morphology of unbundled GaSI crystals. a, HRTEM image of GaSeI with the raw image (left) and the FFT-filtered image (right) included for clarity. Scale bar, 2 nm. b, FFT image of the [100]-oriented micrograph in a. Scale bar, 0.2 $\mbox{Å}^{-1}$. c, Average intensity plot from the FFT-filtered HRTEM of GaSeI. The equivalent crystal structure along

the $[1\,0\,0]$ axis is included for better visualization. \mathbf{d} , AFM of exfoliated GaSel crystals. Scale bar, 200 nm. \mathbf{e} , AFM (left) and corresponding height profiles (right) of exfoliated GaSel. Scale bars, 100 nm (top three micrographs) and 250 nm (bottom micrograph).

radius, pitch, handedness and direction vector of the tetrahelices formed by Ga, Se and I atoms in GaSeI using the atomic positions from the refined single-crystal structure (Supplementary Tables 9 and 10)⁴³. Least-squares fitting also allowed for the extraction of the Ga, Se and I helical meridian angles, α , which is often used to derive the helical radii in nucleic acids from diffraction patterns (Fig. 2f and Supplementary Table 10)^{23,24,44}. This fitted angle of -107° from the helix that is formed by the iodine atoms matches very well with the meridian angle estimated from the experimental single-crystal precession diffraction image along the (0 k l) plane heavily influenced by the heavier I atom (Fig. 2g,h). Aside from the (0 k l) plane, signatures of helicity can be recognized throughout the simulated SCXRD patterns of GaSeI such as the [-1152] direction (highlighted in red), which also corresponds to one of the more prominent Bragg peaks in the ensemble powder X-ray diffraction (PXRD) pattern (Fig. 2h and Supplementary Fig. 1).

High-resolution transmission electron microscopy (HRTEM) of GaSeI demonstrates how the atomic-scale helicity translates into nanoto microscale structures through the long-range ordered rows of 1D chains with spiral/helical contrast arising from the I atoms ordered along the [100] zone axis (Fig. 3a-c and Supplementary Figs. 9 and 10). Fast Fourier transform (FFT) of Fig. 3a accentuates the uniformity of the vdW-stacked chains and the helical ordering as reflected by the similar meridian angle of ~107° (Fig. 3b). The weak interchain vdW interactions in GaSeI enabled us to exfoliate bulk crystals into their nanoscale analogues using traditional micromechanical exfoliation techniques. Atomic force microscopy (AFM) of exfoliated crystals shows an abundance of freestanding GaSeI nanowires in various sizes with no signs of any quasi-2D sheets (Fig. 3d). We show that GaSel can be exfoliated into very thin nanowire bundles with various diameters (Fig. 3e) down to a freestanding 0.9(2)-nm-thick GaSeI structure (Fig. 3e, red borders), equivalent to a single helical chain with approximately 0.96 nm thickness across the helix (d_{002} ; Supplementary Table 8).

Consistently, the highly anisotropic covalent intra- and vdW interchain bonding nature of GaSeI, like in InSeI, is also manifested in the strongly orientation-dependent Raman modes (Supplementary Fig. 11) and axis-specific ambient air stability with respect to the covalent chain axis (Supplementary Figs. 12 and 13). Using micro-Raman spectroscopy as a probe, we found that the single-crystal facets corresponding to the vdW surface (for example (100), (001) or (h0k) facets) were notably more air stable (up to ~2 h) as compared with the perpendicularly cleaved ends of the crystalline needles which are presumably rich in (010) facets (Supplementary Figs. 12 and 13). Like many low-dimensional vdW solids, we attribute this relatively faster degradation rate (<1 h) along the cleaved covalent direction, compared with the vdW surfaces, to the formation of non-passivating dangling bonds that arise from broken covalent bonds along the long chain axis. To emphasize this point, we show that intentionally ground crystallite powders that have a considerably larger fraction of (010) facets are air stable for substantially less than 30 min (Supplementary Figs. 12 and 13).

Establishing the B-C helicity of a 1D vdW material

Unlike its periodic tetrahelix counterparts, the unusual order of the tetrahelices formed by constituent atoms in GaSel gives rise to its space group non-centrosymmetry. As such, we look into the helicity features which distinguish periodic from aperiodic tetrahelices such as: (1) helix rise (h), helix radius (r), tetrahedral edge (a) and the rotational or twist angle (θ_r) (Fig. 4a); (2) distinct vertices from four uniquely oriented polygonal helix-forming tetrahedra defined by equal edge lengths and angles (Fig. 4b, top); (3) subhelix types (Fig. 4b, middle, and Supplementary Text D); and (4) non-repeating vertex arrangement (Fig. 4b, bottom) ^{23–26}. Overlaying the experimental Ga atomic positions from the refined SCXRD structure with the closest ideal B-C helix model based on these attributes revealed a strong agreement of the Ga positions with the B-C helix vertices across 38 tetrahedral units along the defined

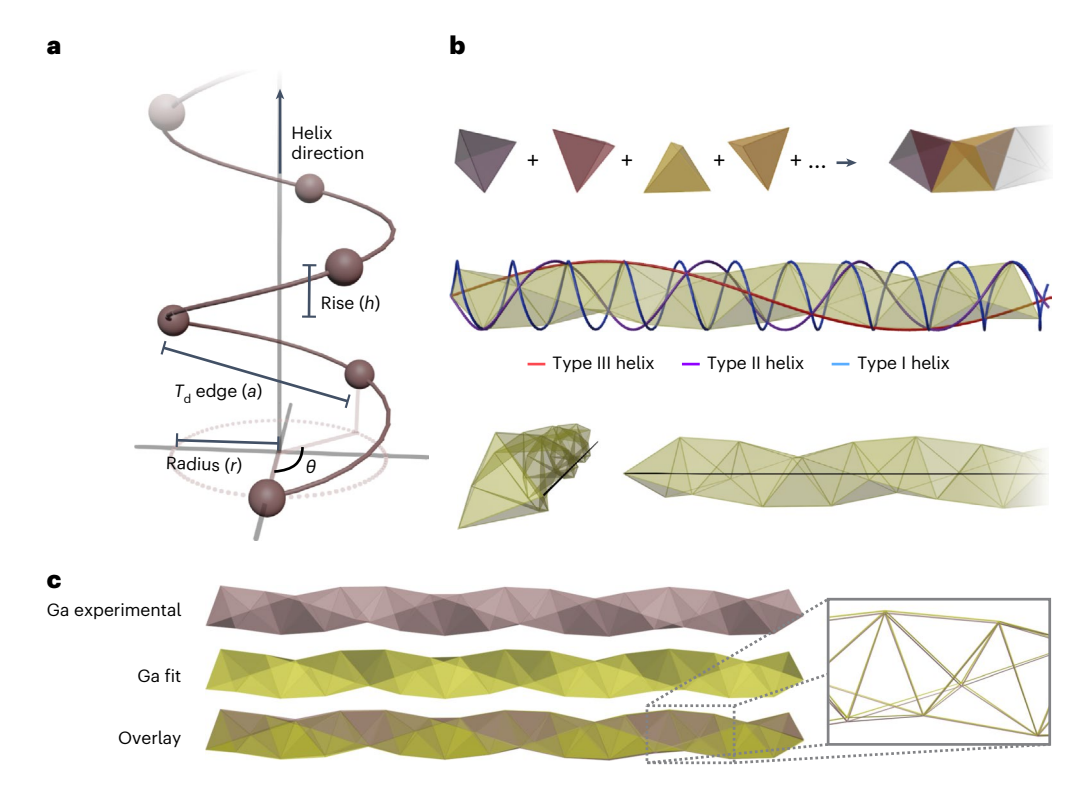


Fig. 4 | Hallmarks of the B-C helix geometry and signatures of B-C helicity in GaSeI. a, Schematic of the B-C helix geometry. b, Aperiodic helical attributes of an ideal R-handed B-C helix. c, Overlay of experimental Ga atom lattice positions in GaSeI represented in brown colour with a corresponding R-handed ideal B-C

helix model in mustard colour across the unit cell (38 tetrahedra and 41 vertices). The highlighted section shows the close agreement of the experimental lattice positions with the ideal B-C helix model.

48.794(4) Å unit-cell length (Fig. 4c). Least-squares regression fitting of the Ga positions to the closest ideal type IB-C helix vertices derived from coordinate/parametric analysis using $x = r \cos n\theta_r$, $y = r \sin n\theta_r$, and z = nh (where n is an arbitrary integer) enabled us to quantitatively establish this close agreement. Direct comparison of the basal, x and z axis, coordinates of the Ga positions with the best-fit ideal B-C helix vertices across n = 41 positions resulted in a linear least-squares fit or R^2_{yz} of 0.9979 and 0.9982 for when the rotational angle was set at cos⁻¹(-2/3) ~131.81...° or when refined as 131.72(2)°, respectively (Fig. 5a, Supplementary Fig. 14 and Supplementary Table 11). Results from these fittings also lie close to the type I helical parameters obtained from HELFIT (Supplementary Tables 9 and 10). Beyond the closeness of the experimental positions to the model, we also highlight the uniform Ga-Ga distances and Ga-Ga-Ga angles in the tetrahedra constituting the Ga helix (Supplementary Fig. 15). This observation conforms to the strict definition of B-C helicity and the validity of our refinement (Supplementary Text F). As expected, employing the same analysis to the coordinates of the In, Se and I4₁ tetrahelices resulted in parameters that do not match an ideal B-C helix but, instead, are better described by a periodic helix with a 135° rotational angle (Supplementary Figs. 16–19 and Supplementary Tables 12-15).

We turn to the local coordination environment to understand the origin of the B-C helicity of Ga atoms and how this influences the helicity of the bound Se and I atoms (Fig. 5b). In GaSeI, the quasi-tetrahedral bonding environment in Ga that radially propagates along the crystallographic long axis suggests that the helical parameters of the tetrahelix formed by Se atoms will be similar to those of Ga, while the tetrahelix formed by I atoms (which radially point out along the basal plane) will have a drastically larger helical radius. Adopting the same coordinate/parametric analysis to the Se and I atomic positions revealed that the helicities of these atoms are dictated by the central Ga atom, wherein the Se and I atoms form concentric B-C helix variants

that are coaxial with the Ga helix but with larger helix radii (Fig. 5c, Supplementary Figs. 20 and 21 and Supplementary Tables 16 and 17). Projection of the helical lattice as a 2D flat strip lattice of the Ga, Se and I helices further illustrates the systematic elongation of the helix radii and contrasts the ideal B-C helicity in Ga, which forms equilateral triangular lattice, from the B-C helix variants in Se and I atoms, which forms calene triangular lattices (Fig. 5d and Supplementary Fig. 15)^{23,24}. While bearing a comparable θ_r with the Ga tetrahelix, we emphasize that the Se and I tetrahelices are non-ideal B-C helix variants due to the concise relationship between r and h in B-C helices that arise from their correlation with the tetrahelix edge length, a, exactly equivalent to

 $r = \frac{3\sqrt{3}}{10}a$ and $h = \frac{1}{\sqrt{10}}a$, respectively (Supplementary Tables 16–18).

Combining these structural observations and B-C helix parameter analyses, we establish that the weak interchain vdW interactions coupled with the minimal electronic reconfiguration arising from isovalent substitution facilitate the structural rearrangement accompanying the conversion of the 135° rotational angle associated with the larger In atom in InSeI to the smaller 131.81...° B-C helix rotational angle of Ga in GaSel. B-C helicity is manifested in GaSel because of the shorter core bond lengths formed by Ga and Se atoms (2.43(7) Å), leading to a smaller rotational angle, in contrast to the In and Se bonding counterpart (2.619(8) Å) in InSeI (Supplementary Table 19). Surprisingly, extraction of the axial bond angles in the $[GaSe_3I]_{\infty}$ and $[SeGa_3]_{\infty}$ units show a closer adherence to the ideal 109.5° and 90 < θ < 109.5° angles formed by tetrahedral and trigonal pyramidal geometries, compared with their counterparts in InSeI indicating a more efficient polyhedral packing order that is consistent with B-C helicity (Fig. 5b and Supplementary Table 19). These observations suggest that the key parameter dictating the nature of the tetrahelix lies within the structure of the tetrahedral building blocks. While the observed Ga-I and Ga-Se bond lengths are comparable to their binary tetrahedral counterparts 45,46, it is the overall

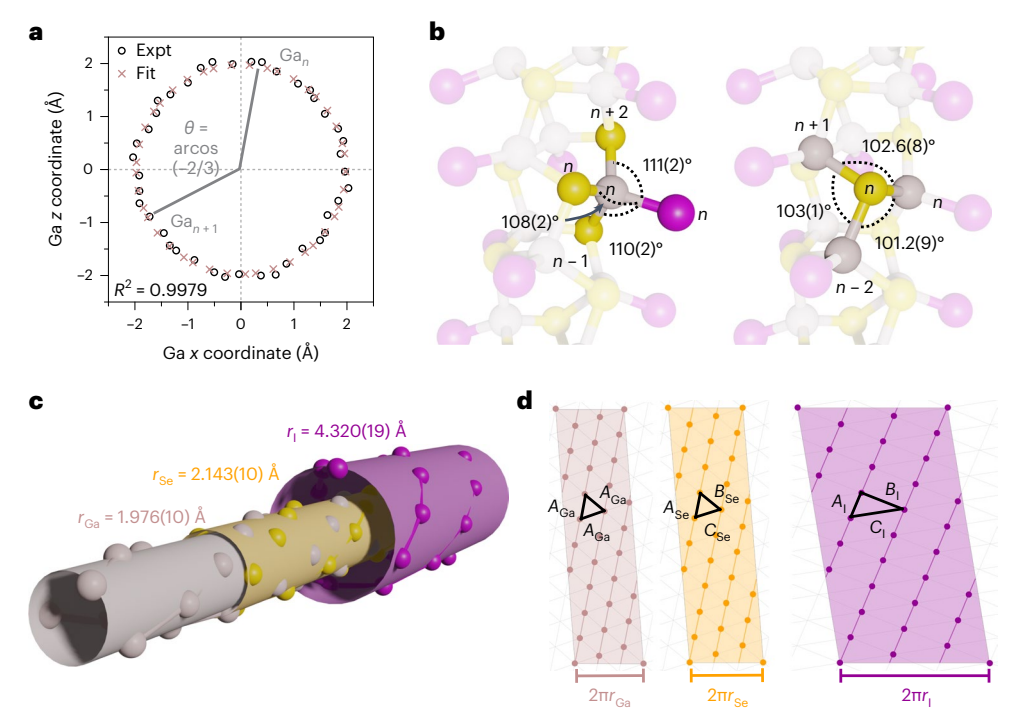


Fig. 5 | **B-C helix parameters and origin of B-C helicity in GaSel. a**, B-C helix coordinate and parametric analysis of the experimental (Expt) z- and x-coordinate positions of Ga atoms (vertex, n = 41). The irrational B-C helix twist angle between Ga_n and Ga_{n+1} is depicted in the graph. **b**, Average experimental bond angles around quasi-tetrahedrally coordinated Ga atoms ([GaSe₃I] $_{\infty}$ unit)

and quasi-trigonal pyramidal coordinated Se atoms ($[SeGa_3]_{\infty}$ unit) in GaSel. **c**, Helices formed by Ga, Se and I atoms in GaSel represented as concentric cylinders with varying helical radii. **d**, Flat strip projection of the Ga, Se and I helices tiled with equilateral (Ga) and scalene (Se, I) triangles.

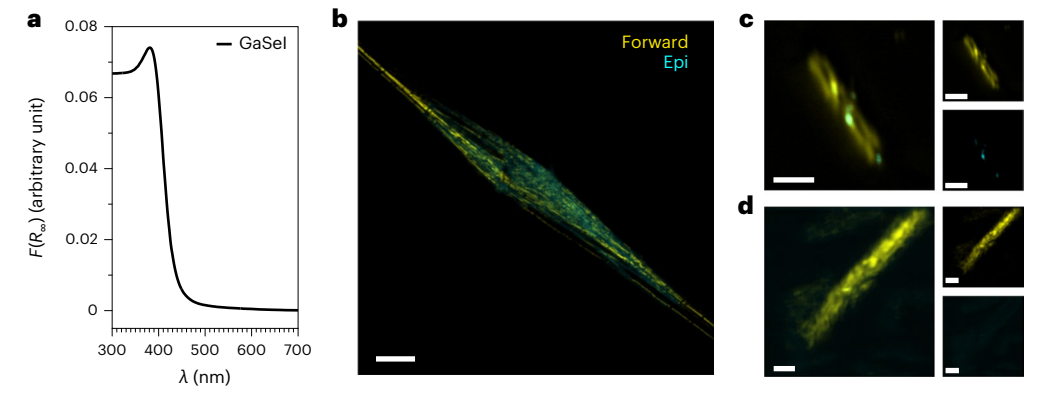


Fig. 6 | **Optical spectroscopy of GaSel microcrystallites. a**, DRS spectrum of GaSel microcrystallites plotted in terms of the KM function, $F(R_{\infty})$. **b**, Composite SHG optical micrograph in the forward and epi channels of an intentionally fanned out GaSel crystal via micromechanical force (setup 1 in Methods and Supplementary Fig. 23). Scale bar, 20 μ m. **c**, Composite SHG optical

micrograph of a thin exfoliated GaSel microcrystallite (setup 2 in Methods and Supplementary Fig. 23). \mathbf{d} , Composite SHG optical micrographs of a wider and longer exfoliated GaSel microcrystallite (setup 2 in Methods and Supplementary Fig. 23). Constituent forward (top) and epi (bottom) channels of the composite micrographs are shown in \mathbf{c} (right) and \mathbf{d} (right). Scale bars, $2 \, \mu m$.

coordination nature of the [GaSe $_3$ l] quasi-tetrahedral structure that drives the formation of the B-C helix. Particularly, the terminating iodine atom induces the 1D crystallization of the quasi-tetrahedral building units while the Ga–Se bonds ideally bridge the units to induce the expression of the irrational twist angle. Identifying features and general materials design considerations of B-C helices are discussed in Supplementary Text G.

Optical properties of GaSel

Finally, we probed the optical properties of GaSel crystals to understand the influence of helicity on the electronic and optical states III–VI–VII crystals. Room-temperature diffuse reflectance spectroscopy

(DRS) of GaSel microcrystallites under inert conditions and plotted in terms of the Kubelka–Munk (KM) function, $F(R_{\infty})$, shows a sharp absorption onset corresponding to an estimated bandgap energy, E_g , of 2.85 eV (435 nm) (maximum of the first derivative plot is centred at 3.03 eV; Fig. 6a and Supplementary Fig. 22). Compared with InSel (Supplementary Fig. 22), the absorption onset of GaSel is notably blue shifted by about 0.4 eV, consistent with the stronger orbital overlap in the quasi-tetrahedral building unit arising from the smaller central Ga atom. While racemic, the non-centrosymmetric Cc space group of GaSel presented an opportunity to probe the prospects of optical nonlinearity arising from the packing of the constituent B-C helical chains crystallographically defined by glide planes that run parallel to the long axis

of the chains and impart non-centrosymmetry. Room-temperature second harmonic generation (SHG) microscopy of GaSel shows pronounced SHG intensities, directly confirming the absence of inversion symmetry in the bulk crystal (Fig. 6b–d and Supplementary Fig. 23) 47 . These robust and well-resolved SHG micrographs, intriguingly, revealed the underlying fibrous nature of the crystal microstructure for both the bulk (Fig. 6b) and micrometre-sized crystallites (Fig. 6c,d). This observation of SHG in pristine and intentionally deformed crystals is consistent with the Cc space group (m point group) and multiple reports of optical activity in 3D extended lattice crystals with space groups defined by non-centrosymmetric racemate motifs like those having m, mm2, -4 and -42m point groups 48 (Fig. 6).

Outlook

Broadly, the manifestation of ideal B-C helicity in 1D vdW tetrahelices underscores the potential for this emergent class of vdW helices to understand the fundamental relationship between helicity and structural aperiodicity in the packing of 1D condensed phases. The structural degree of freedom that enabled us to access GaSeI from InSel can be further harnessed as a general strategy to create aperiodic low-dimensional materials with tunable helical parameters that span a broad range of physical properties. Realizing the full potential of chirality in these motifs would, however, require drastic advances in bulk, top-down and bottom-up synthetic strategies to create enantiopure assemblies. Chemical vapour deposition, selective facet exfoliation and polytype engineering should be rational first objectives towards achieving this goal. Still, we should also not underestimate racemic assemblies either, as nascent properties have also developed from global instead of local symmetry, such as ultrafast directional photoconductivity⁴⁹, topologically protected nodal ring phononic states⁸ and topological Fermi arcs⁵⁰. The emerging role of helical motifs and structures in a multitude of emergent physical phenomena makes this class of III-VI-VII 1D vdW helices a candidate material platform to systematically probe the anticipated physics concomitant with periodic and aperiodic helicity in dense solid-state structures.

Online content

Any methods, additional references, Nature Portfolio reporting summaries, source data, extended data, supplementary information, acknowledgements, peer review information; details of author contributions and competing interests; and statements of data and code availability are available at https://doi.org/10.1038/s41563-024-01963-4.

References

- Moser, H. E. & Dervan, P. B. Sequence-specific cleavage of double helical DNA by triple helix formation. Science 238, 645–650 (1987).
- Douglas, S. M. et al. Self-assembly of DNA into nanoscale three-dimensional shapes. Nature 459, 414–418 (2009).
- Hirschberg, J. et al. Helical self-assembled polymers from cooperative stacking of hydrogen-bonded pairs. *Nature* 407, 167–170 (2000).
- Naaman, R. & Waldeck, D. H. Spintronics and chirality: spin selectivity in electron transport through chiral molecules. Annu. Rev. Phys. Chem. 66, 263–281 (2015).
- Kuzyk, A. et al. DNA-based self-assembly of chiral plasmonic nanostructures with tailored optical response. *Nature* 483, 311–314 (2012).
- Chang, G. Q. et al. Topological quantum properties of chiral crystals. Nat. Mater. 17, 978–985 (2018).
- 7. Liu, Y. Z., Xiao, J., Koo, J. & Yan, B. Chirality-driven topological electronic structure of DNA-like materials. *Nat. Mater.* **20**, 638–644 (2021).
- Peng, B., Murakami, S., Monserrat, B. & Zhang, T. Degenerate topological line surface phonons in quasi-1D double helix crystal SnIP. NPJ Comput. Mater. 7, 195 (2021).

- Bierman, M. J. et al. Dislocation-driven nanowire growth and Eshelby twist. Science 320, 1060-1063 (2008).
- Liu, Y. et al. Helical van der Waals crystals with discretized Eshelby twist. Nature 570, 358–362 (2019).
- Zhu, J. et al. Formation of chiral branched nanowires by the Eshelby twist. Nat. Nanotechnol. 3, 477–481 (2008).
- Gao, P. X. et al. Conversion of zinc oxide nanobelts into superlattice-structured nanohelices. Science 309, 1700–1704 (2005).
- Nagaoka, Y. et al. Superstructures generated from truncated tetrahedral quantum dots. *Nature* 561, 378–382 (2018).
- Zhang, L. M. et al. Three-dimensional spirals of atomic layered MoS₂. Nano Lett. 14, 6418–6423 (2014).
- Pfister, D. et al. Inorganic double helices in semiconducting SnIP. Adv. Mater. 28, 9783–9791 (2016).
- Reiter, F. et al. SnBrP-A SnIP-type representative in the Sn-Br-P system. Z. Anorg. Allg. Chem. 648, e202100347 (2022).
- 17. Müller, U. Die symmetrie von Spiralketten. *Acta Crystallogr. Sect. B* **73**, 443–452 (2017).
- Bette, S. et al. Corrosion of heritage objects: collagen-like triple helix found in the calcium acetate hemihydrate crystal structure. Angew. Chem. Int. Ed. 59, 9438–9442 (2020).
- Xiao, Q. et al. A metal-organic framework with rod secondary building unit based on the Boerdijk-Coxeter helix. *Chem. Commun.* 52, 11543–11546 (2016).
- 20. Hartl, H. et al. $[(C_6H_5)_4P]^{1}\infty[Cu_3l_4]$ —the first compound with a helical chain of face-sharing tetrahedra as a structural element. *Angew. Chem. Int. Ed.* **33**, 1841–1842 (1994).
- 21. Berisio, R., Vitagliano, L., Mazzarella, L. & Zagari, A. Crystal structure of the collagen triple helix model [(Pro-Pro-Gly)₁₀]₃. *Protein Sci.* **11**, 262–270 (2002).
- 22. Zheng, C., Hoffmann, R. & Nelson, D. R. A helical face-sharing tetrahedron chain with irrational twist, stella-quadrangula, and related matters. *J. Am. Chem.* Soc. **112**, 3784–3791 (1990).
- 23. Sadoc, J. F. & Rivier, N. Boerdijk-Coxeter helix and biological helices. *Eur. Phys. J. B* **12**, 309–318 (1999).
- Sadoc, J. F. & Rivier, N. Boerdijk–Coxeter helix and biological helices as quasicrystals. *Mater. Sci. Eng. A* 294–296, 397–400 (2000).
- Zhu, Y. H. et al. Chiral gold nanowires with Boerdijk-Coxeter– Bernal structure. J. Am. Chem. Soc. 136. 12746–12752 (2014).
- Lord, E. A., Mackay, A. L. & Ranganathan, S. New Geometries for New Materials (Cambridge Univ. Press, 2006).
- 27. Fuller, R. B. Synergetics: Explorations in the Geometry of Thinking (Estate of R. Buckminster Fuller, 1982).
- Vardeny, Z. V., Nahata, A. & Agrawal, A. Optics of photonic quasicrystals. *Nat. Photonics* 7, 177–187 (2013).
- Hu, R. & Tian, Z. Direct observation of phonon Anderson localization in Si/Ge aperiodic superlattices. *Phys. Rev. B* 103, 045304 (2021).
- 30. Silva, J., Vasconcelos, M. S., Anselmo, D. H. A. L. & Mello, V. D. Phononic topological states in 1D quasicrystals. *J. Phys. Condens. Matter* **31**, 505405 (2019).
- 31. Balandin, A. A. et al. One-dimensional van der Waals quantum materials. *Mater. Today* **55**, 74–91 (2022).
- Sawitzki, G. et al. Crystal structures of InTel and InSel. Mater. Res. Bull. 15, 753–762 (1980).
- 33. Kniep, R. et al. Phasenbeziehungen und intermediäre Verbindungen in Systemen $GaX_3-Ga_2S_3$ und $InX_3-In_2S_3$ (X = Cl, Br, I)/ Phase relations and intermediate compounds in systems $GaX_3-Ga_2S_3$ and $InX_3-In_2S_3$ (X = Cl, Br, I). Z. Naturforsch. B **40**, 26–31 (1985).
- Jiang, S. et al. Computational prediction of a novel 1D InSel nanochain with high stability and promising wide-bandgap properties. *Phys. Chem. Chem. Phys.* 22, 27441–27449 (2020).

- 35. Chen, W. et al. Anisotropic correlation between the piezoelectricity and anion-polarizability difference in 2D phosphorene-type ternary GaXY (X = Se, Te; Y = F, Cl, Br, I) monolayers. *J. Mater. Sci.* **56**, 8024–8036 (2021).
- Sasmito, S. A., Anshory, M, Jihad, I. & Absor, M. A. U. Reversible spin textures with giant spin splitting in two-dimensional GaXY (X = Se, Te; Y= Cl, Br, I) compounds for a persistent spin helix. *Phys. Rev. B* 104, 115145 (2021).
- Zhang, S.-H. & Liu, B.-G. A controllable robust multiferroic GaTeCl monolayer with colossal 2D ferroelectricity and desirable multifunctionality. *Nanoscale* 10, 5990–5996 (2018).
- Cordova, D. L. M. et al. Sensitive thermochromic behavior of InSel, a highly anisotropic and tubular 1D van der Waals Crystal. Adv. Mater. 36, 2312597 (2024).
- Zhou, Y. et al. Higher-dimensional spin selectivity in chiral crystals. Preprint at https://arxiv.org/abs/2305.18637v1 (2023).
- 40. Zhao, S. et al. Chirality-induced spin splitting in 1D InSel. *Appl. Phys. Lett.* **123**, 172404 (2023).
- 41. Choi, K. H. et al. One-dimensional van der Waals material InSel with large band-gap for optoelectronic applications. *J. Alloy Compd.* **927**, 166995 (2022).
- Pielmeier, M. R., Karttunen, A. J. & Nilges, T. Toward atomic-scale inorganic double helices via carbon nanotube matrices induction of chirality to carbon nanotubes. J. Phys. Chem. C 124, 13338–13347 (2020).
- 43. Enkhbayar, P., Damdinsuren, S., Osaki, M. & Matsushima, N. HELFIT: helix fitting by a total least squares method. *Comput. Biol. Chem.* **32**, 307–310 (2008).

- 44. Lucas, A. A. & Lambin, P. Diffraction by DNA, carbon nanotubes and other helical nanostructures. *Rep. Prog. Phys.* **68**, 1181–1249 (2005).
- Troyanov, S. I., Krahl, T. & Kemnitz, E. Crystal structures of GaX₃ (X = Cl, Br, I) and All₃. Z. Kristallogr. Crystal. Mater. 219, 88–92 (2004).
- 46. Kuhn, A., Chevy, A. & Chevalier, R. Crystal structure and interatomic distances in GaSe. *Phys. Status Solidi A* **31**, 469–475 (1975).
- Bonacina, L., Brevet, P.-F., Finazzi, M. & Celebrano, M. Harmonic generation at the nanoscale. J. Appl. Phys. 127, 230901 (2020).
- 48. Gautier, R., Klingsporn, J. M., Van Duyne, R. P. & Poeppelmeier, K. R. Optical activity from racemates. *Nat. Mater.* **15**, 591–592 (2016).
- Purschke, D. N. et al. Ultrafast photoconductivity and terahertz vibrational dynamics in double-helix SnIP nanowires. *Adv. Mater.* 33, 2100978 (2021).
- 50. Mathur, N. et al. Atomically sharp internal interface in a chiral weyl semimetal nanowire. *Nano Lett.* **23**, 2695–2702 (2023).

Publisher's note Springer Nature remains neutral with regard to jurisdictional claims in published maps and institutional affiliations.

Springer Nature or its licensor (e.g. a society or other partner) holds exclusive rights to this article under a publishing agreement with the author(s) or other rightsholder(s); author self-archiving of the accepted manuscript version of this article is solely governed by the terms of such publishing agreement and applicable law.

© The Author(s), under exclusive licence to Springer Nature Limited 2024

Methods

Materials preparation and handling

All commercially available materials were used as received unless otherwise noted. All air- and water-sensitive samples were stored inside an Ar-filled glove box when not in use. During loading onto characterization instruments, the air exposure of GaSel single crystals was minimized and lasted well below its determined decomposition period.

CVT synthesis of GaSeI

GaSel was grown using a CVT technique. Ga (STREM Chemicals, 99.99%), Se (STREM Chemicals, 99.5%) and $\rm I_2$ (Spectrum Chemical, 99.8%) in a 1:1:1 Ga:Se:I ratio were vacuum sealed to <20 mTorr pressure in a Pyrex ampoule and placed in a horizontal two-zone furnace. The precursor side and deposition side were heated to 500 °C and 450 °C, respectively. The reaction temperatures were held for 7 days and slowly cooled to room temperature for 7 days.

Melt synthesis of InSel

InSel was grown via melt synthesis. In (STREM Chemicals, 99.9%), Se (STREM Chemicals, 99.5%) and $\rm I_2$ (Spectrum Chemical, 99.8%) in a 1:1:1 In:Se:I ratio were vacuum sealed to <20 mTorr pressure in a Pyrex ampoule and placed in a horizontal two-zone furnace. Both zones were heated to 450 °C and were held for 4 days. The reaction was then cooled to room temperature for 1 day.

Micromechanical exfoliation of GaSeI

GaSel crystals were micromechanically exfoliated by orienting single crystals in one direction onto a small piece of polydimethylsiloxane (PDMS) gel and smearing onto another piece of PDMS gel along the long axis of the crystals. The resulting exfoliated crystals were stamped onto various surfaces depending on the characterization method.

PXRD

PXRD was conducted on a Rigaku MiniFlex 600 with a Cu K α source at a voltage of 40 kV and current of 15 mA. For the ensemble measurements of single crystals, bundles of GaSel crystals were placed on a sample holder and flattened to create a uniform surface. Simulated PXRD patterns were generated using CrystalDiffract software.

Optical microscopy

High-magnification (up to $\times 100$) optical images of single and exfoliated crystals were collected on an Olympus BX43F microscope with bright-field and dark-field capabilities.

$\label{eq:scxrd} \textbf{SCXRD} \ \textbf{data} \ \textbf{collection}, \textbf{structure} \ \textbf{solution} \ \textbf{and} \ \textbf{refinement} \ \textbf{for} \\ \textbf{GaSeI}$

The single crystals of GaSeI used in the SCXRD experiment were kept in an Ar glovebox until before the measurement. Before the crystals were taken out of the inert environment, they were covered in paraffin oil to prevent disruptive collision or mechanical abrasion with adjacent crystals. Suitable crystals were painstakingly selected and carefully handled while being transferred to the cryoloop. To prevent further damage, the crystal was not cleaved nor contacted; only the surrounding paraffin oil was manipulated.

A colourless needle-shaped crystal of approximate dimensions $0.694 \times 0.036 \times 0.032$ mm was mounted in a cryoloop and transferred to a Bruker SMART APEX II diffractometer system. The APEX3 (ref. 51) program package was used to determine the unit-cell parameters and for data collection (5–10 s per frame scan time). The APEX4 (ref. 52) program package was used for further data analysis. The raw frame data were processed using SAINT⁵³ and SADABS⁵⁴ with face-indexed absorption correction applied, yielding a refined μ value of 27.708 mm⁻¹. No additional absorption corrections were applied. Subsequent calculations were carried out using the SHELXTL⁵⁵ program package using the Olex 1.5 (ref. 56) graphical user interface. The diffraction symmetry

was 2/m, and the systematic absences were consistent with the monoclinic space groups Cc and C2/c. It was later determined that space group Cc was correct with diffraction symmetry of m.

The structure was solved by direct methods and refined on F^2 by full-matrix least-squares techniques. The analytical scattering factors for neutral atoms were used throughout the analysis. Refinement of the structure yielded a Flack parameter for 0.503(13), which is consistent with the presence of both the L- and R-handed helices present in this structure. Refinement as an inversion twin yielded a Hooft parameter of -0.005(8) indicating good agreement of the assignment of this structure as an inversion twin rather than having a missed inversion centre. Doubled spots at high angles indicate that this is a pseudo-merohedral inversion twin.

Least-squares analysis yielded wR2 of 0.1496 and GooF of 1.023 for 1,108 variables refined against 31795 data (0.8257 Å), R1 of 0.0542 for those 23,401 data with $I > 2.0\sigma(I)$.

To ensure the robustness of the raw data, the frames were independently re-integrated, resolved and refined to the same Cc space group and asymmetric structure as before. The new refinement yielded a slight improvement in the RI, wR2 and $R_{\rm int}$ values and produced only minor G-alerts from the checkcif validation. The inclusion of an inversion twin in the refinement was still necessary.

Definitions:

wR2 =
$$\left[\Sigma \left[w(F_0^2 - F_c^2)^2\right] / \Sigma \left[w(F_0^2)^2\right]\right]^{1/2}$$

$$R1 = \Sigma ||F_{\rm o}| - |F_{\rm c}|| / \sum |F_{\rm o}|$$

GooF =
$$S = \left[\sum \left[w(F_o^2 - F_c^2)^2\right]/(n-p)\right]^{1/2}$$
, where n is the number of

reflections and p is the total number of parameters refined.

The thermal ellipsoid plot is shown at the 99% probability level (Supplementary Fig. 4).

HRTEM

HRTEM images were acquired using a JEOL JEM 2800 and Grand ARM 300CF S/TEMs operated at an accelerating voltage of 200 kV equipped with a Schottky-type field emission electron source, annular dark-field detector, 100 mm² silicon drift detector for EDS, selected area electron diffraction capabilities and Gatan OneView 4K and Gatan K2 cameras with drift correction. Samples were prepared by smearing lacey carbon transmission electron microscopy (TEM) grids (200 mesh, Ted Pella) onto exfoliated GaSel crystals on PMDS gel. Because of the limited thermal stability of GaSeI, beam damage to the sample was minimized as much as possible by using low dose parameters. To minimize beam damage on the region of interest (ROI), an adjacent region was first focused. Then, the electron beam was blanked and moved to the ROI. Immediately after moving to the ROI, the beam was turned on and image collection was started. Analysis of raw HRTEM data (.dm4) was done using Gatan OneView software. FFT and intensity profile analysis were done using ImageJ software. FFT filtering of HRTEM image was done on ImageJ by optimizing the contrast on the FFT data by adjusting the window/level sliders and then recalculating the resulting filtered image by inverse FFT. Indexing of selected area electron diffraction and FFT data was performed using SingleCrystal software.

Extensive twinning features are observed in the TEM data because of the very weak interaction between individual chains in the crystal structure. Any small physical perturbation could dislodge and shift crystal domains and induce structural changes that have the same effect as twinning in electron diffraction and FFT of HRTEM images. To prepare samples with suitable thinness for TEM, single crystals were gently spread across a PDMS gel to achieve exfoliation. Then, TEM grids were gently contacted on the gel surface to transfer the exfoliated crystals.

SEM and EDS

SEM images and EDS analysis using an FEI Magellan 400 XHR SEM, equipped with an ETD detector and 80 mm² Oxford silicon drift EDS detector. Imaging and EDS analysis were done at an operating voltage of 10–20 kV and current of at least 1 nA.

AFM

AFM images were collected on an Anton Paar Tosca 400 AFM using non-contact mode Arrow silicon SPM-sensor tips with a nominal tip size of 10 nm, resonance frequency of 285 kHz and force constant of 42 N m $^{-1}$. To prepare samples, single crystals of GaSel were exfoliated by repeatedly pressing crystals between two pieces of PDMS gel. After good coverage of the gel was achieved, the exfoliated crystals were stamped onto 285 nm SiO $_2$ /Si substrate with fiduciary marks.

Raman spectroscopy

Raman spectra of GaSel and InSel single crystals were collected on a Raman system based on the Renishaw Invia microscope equipped with a 532 nmlaser. The polarization of the 532 nmlaser runs along the horizontal line of the crosshairs on the microscopy image. Large single crystals were identified and aligned either parallel or perpendicular with respect to the laser polarization. Raman measurements were performed with a nominal power of 0.103 mW, 10 s exposure time and one to five accumulations. For the time-dependent Raman studies, 1 s exposure time was used.

DRS

Diffuse reflectance measurements were performed on a Jasco V-670 spectrometer equipped with a 60 mm integrating sphere (Jasco ISN-923) operating at a working range of 190–2,500 nm. Single crystals were ground and dispersed in KBr to yield a -1–5% w/w mixture. The resulting mixture was loaded and slightly compressed onto a custom-made holder with a transparent quartz window.

TGA

TGA was performed using a TA Instruments Thermogravimetric Analyzer Q500 at a heating rate of 10 °C min⁻¹ from 20 °C to 900 °C while being purged with N_2 gas at a flow rate of 50 ml min⁻¹. A bundle of single crystals was placed on a platinum pan during the analysis.

XPS

XPS measurements were conducted on a Kratos Analytical Axis Supra spectrometer equipped with a dual source Al/Ag monochromatic X-ray source with a spot size of approximately 500- μ m-diameter circle. Single crystals of GaSel were mounted onto a dual-height sample holder using carbon tape. Fitting of XPS spectra was accomplished using CasaXPS software.

Least-squares fitting of tetrahelix and B-C helix parameters

A least-squares regression analysis was performed using GraphPad Prism on atomic coordinates derived from the single-crystal structure to determine the best tetrahelix fit for the group III, VI and VII elements in a single vdW chain. Starting with the experimental crystal structures, the unit-cell boundaries were reduced so that only a single chain is present. The unit-cell origins were shifted so a single chain is centred at the origin. For GaSeI, the original unit cell was recentred so that the origin is at ($\frac{1}{2}$, 0, $\frac{1}{2}$) and the boundary was set to $-\frac{1}{4} \le a \le \frac{1}{4}$, $0 \le b \le 1$ and $-\frac{1}{4} \le c \le \frac{1}{4}$. For InSeI, the boundary was set to $0 \le a \le \frac{1}{2}$, $\frac{1}{4} \le b \le \frac{3}{4}$ and $0 \le c \le 3$. The fractional coordinates were then converted to Cartesian coordinates using VESTA software. From the Cartesian coordinates of the M (Ga, In) and Se atoms, the best tetrahelix was fit using

$$x = r \cos(\theta_{i} + k\theta_{r})$$

$$y = \pm r \sin(\theta_{i} + k\theta_{r}) ,$$

$$z = h_{i} + kh$$

where r is the radius of the cylinder bound by the tetrahelix, θ_r is the angle between two adjacent vertices around the tetrahelix axis, θ_i is an angle shift to account for the initial starting position along the basal plane, h is the rise or the vertical distance along the axis between vertices, h_i is the vertical position of the first point, and k is an integer. For the calculations, the tetrahelix axis (z direction) is the b axis for GaSel and the c axis for InSel. Least-squares regression analysis was used to refine the best-fit tetrahelix for each single-chain structure.

SHG microscopy

SHG microscopy has been performed using the fundamental output of a femtosecond oscillator (MaiTai, Spectra Physics) coupled into an Olympus FluoView 1000 laser scanning microscopy system based on an Olympus IX81 inverted microscope frame. Two slightly different experimental conditions and optical arrangements have been used. For setup 1, the fundamental pulse at 760 nm (80 fs, 76 MHz, 10 mW) was coupled onto a 60× numerical aperture 1.41 oil-immersion objective lens (Olympus) by 697 nm short-pass dichroic mirror. In the epi direction, the SHG signal is transmitted though the same coupling mirror and further filtered using UG5 filter before being detected by photomultiplier tube (Hamamatsu). In the forward direction, the SHG signal was collected by a condenser lens and reflected/filtered by the combination of 409 nm long-pass dichroic mirror (Semrock) and UG11 colour filter (Schott) onto a similar photomultiplier tube (Hamamatsu). For setup 2, 800 nm (80 fs, 76 MHz, 10 mW) was used as the excitation wavelength with a 720 nm short-pass dichroic mirror (Semrock) as the coupling mirror. BG40 and BG38 glass filters (Schott) were used in epi and forward channel, respectively, to further filter the generated signal. Imaging was performed at various fields of view with nominal resolutions of 800×800 and $2,048 \times 2,048$ pixels with scanning speed set at 2 µs per pixel.

Extraction of single helix parameters using HELFIT

The helical parameters of GaSel were calculated using HELFIT software 43 . HELFIT uses least-squares fitting to determine the helix radius, pitch, handedness and direction vector. Atomic positions were first converted from fractional coordinates into Cartesian coordinates using VESTA software. The coordinates of the three helices from each element were assigned via inspection of the *y*-axis coordinates. The coordinates of a single elemental helix covering a span of one unit cell were used as the input information for the software (for example, gallium.txt). The helix meridian angle (a) was calculated using

$$a=2\pi rP$$
,

where r is the helix radius and P is the helix pitch.

Data availability

Crystallographic data can be obtained free of charge from the Cambridge Crystallographic Data Centre (CCDC) via www.ccdc.cam.ac.uk/data_request/cif (CCDC deposition no. 2360595). All other data supporting the findings of this study are available within the Article and its Supplementary Information. Any additional material is available from the corresponding author upon reasonable request.

References

- 51. APEX3 Version 2014.11-0 (Bruker AXS, 2014).
- 52. APEX4 Version 2021.4-0 (Bruker AXS, 2021).
- 53. SAINT Version 8.40B (Bruker AXS, 2013).
- 54. SADABS, Version 2016/2 (Bruker AXS, 2016).
- 55. SHELXTL, Version 2019/1 (Bruker AXS, 2019).
- Dolomanov, O. V. et al. OLEX2: a complete structure solution, refinement and analysis program. J. Appl. Crystallogr. 42, 339–341 (2009).

- Prince, E. International Tables for Crystallography, Volume C: Mathematical, Physical and Chemical Tables (Springer Science & Business Media, 2004).
- 58. Flack, H. On enantiomorph-polarity estimation. *Acta Crystallogr.* Sect. A **39**, 876–881 (1983).
- Hooft, R. W., Straver, L. H. & Spek, A. L. Determination of absolute structure using Bayesian statistics on Bijvoet differences. *J. Appl. Crystallogr.* 41, 96–103 (2008).

Acknowledgements

We thank the UC Irvine Department of Chemistry X-ray crystallography facility for the instrumental support on the single-crystal diffraction experiments. T.A.K. and J.Z. acknowledge the UC Irvine School of Physical Sciences and Department of Chemistry for funding. We also thank the UC Irvine Laser Spectroscopy Labs. D.A.F. acknowledges support through NIH GM R21-GM141774. Several aspects of this work were performed at the UC Irvine Materials Research Institute (IMRI). Facilities and instrumentation at IMRI are supported, in part, by the National Science Foundation through the UC Irvine Materials Research Science and Engineering Center grant number DMR-2011967. XPS was performed using instrumentation funded in part by the National Science Foundation Major Research Instrumentation Program under grant number CHE-1338173. AFM was performed using an Anton Paar Tosca 400 AFM on loan to IMRI from Anton Paar GmbH.

Author contributions

Conceptualization: M.Q.A. Methodology: D.L.M.C., K.C., G.S., D.A.F. and M.Q.A. Investigation: D.L.M.C., K.C., T.A.K., T.A., D.K., D.L. and D.A.F. Visualization: D.L.M.C., K.C., D.A.F. and M.Q.A. Funding acquisition: M.Q.A. Project administration: M.Q.A. Supervision: M.Q.A. Writing—original draft: D.L.M.C., K.C. and M.Q.A. Writing—review and editing: D.L.M.C., K.C., T.A.K., T.A., D.K., G.S., D.L., J.Z., D.A.F. and M.Q.A.

Competing interests

The authors declare no competing interests.

Additional information

Supplementary information The online version contains supplementary material available at https://doi.org/10.1038/s41563-024-01963-4.

Correspondence and requests for materials should be addressed to Maxx Q. Arguilla.

Peer review information *Nature Materials* thanks Jan Ingo Flege, Tom Nilges, Binghai Yan and the other, anonymous, reviewer(s) for their contribution to the peer review of this work.

Reprints and permissions information is available at www.nature.com/reprints.